Sensors & Diagnostics

ROYAL SOCIETY OF CHEMISTRY

PAPER

View Article Online
View Journal | View Issue

Check for updates

Cite this: *Sens. Diagn.*, 2022, **1**, 177

Colorimetric assay based on iron(III) ions triggering the aggregation of a poly(tannic acid) coated Au nanocomposite for carbonic anhydrase II detection†

Jiale Pan,[a] Junjiao Yang, [b] Shiman Yao[a] and Jing Yang *[a]

Received 3rd September 2021,
Accepted 29th September 2021

DOI: 10.1039/d1sd00015b

rsc.li/sensors

Herein, several components including mesoporous silica nanoparticles (MSNs) as a reservoir to load iron(III) ions for triggering a color change and a gold nanoparticle (AuNP) as an imaging agent prepared and stabilized using poly(tannic acid) (PTA) were combined together to successfully construct a kind of colorimetric assay for detection of protein. Iron(III) ion-loaded MSNs with an amine-modified surface were capped with the probe-labelled PTA-based shell@core AuNP (AuNP@PTA) through electrostatic interaction, forming probe-labelled PEGylated AuNP@PTA@Fe^{3+}-loaded MSNs. The stronger interaction of the target analyte and the probe molecule would pull the gatekeeper AuNP@PTA away from the surface of the MSNs. The released iron(III) ion would coordinate with PTA, leading to AuNP aggregation for a visual color change. In this study, isozyme carbonic anhydrase II (CA II) and 4-sulfonamidebenzoic acid (SABA) were selected as the protein analyte and probe molecule. The SABA-labelled PEGylated AuNP@PTA@Fe^{3+}-loaded MSNs showed good recognition specificity and sensitivity towards CA II with a visual detection limit of 50 nM, and the limit of detection (LOD) for the AuNP@PTA@Fe^{3+}-loaded MSNs was about 15 nM using a signal-to-noise ratio of 3 with a UV-vis technique. Such proposed nanocomposites exhibited great potential as sensors in medical diagnostics and biological systems without the need for any separation process.

Introduction

Simple and convenient technologies for the identification of chemical and biological species are of great significance for public safety and disease diagnosis.[1,2] However, developing rapid and cost-effective detection techniques with high sensitivity and specificity is always challenging. Compared with various detection methods relying on professional and sophisticated analysis instrumentation,[3–7] colorimetric assays, which are easy to monitor with the naked eye, are constantly improved for satisfactory home-testing or on-site detection.[8–12] For this assay, numerous types of sensors such as Au nanoparticles,[13–16] quantum dots[17,18] and silver nanoparticles[19,20] have been explored.

Gold nanoparticle (AuNP)-based colorimetric sensors are the most researched and broadly applied nanomaterials. Due to their unique features, such as complex optical properties and versatile surface chemistry,[21,22] AuNP-based colorimetric approaches have resulted in a dramatic increase in the efficient detection of biological target[23,24] and small molecules.[25,26] With rapid development of AuNPs, the green synthesis of AuNPs by using a diverse set of biological entities to replace toxic chemicals has attracted tremendous attention. Tannic acid (TA) is a pure natural polyphenolic compound that is abundant in red wine, coffee, green tea and immature fruits.[27] Reductive TA has been successfully used in heating-free green synthesis of metal nanoparticles including AuNPs.[28–30] Moreover, such polyphenolic materials can form a poly(tannic acid) (PTA) shell *via* oxidative self-polymerization to keep the AuNPs stable and non-agglomerated in an aqueous environment (AuNP@PTA).[31] Because the strong coordination interaction between iron(III) ions (Fe^{3+}) and PTA can trigger the aggregation of AuNPs, AuNP@PTA has been developed for a simple and highly visual method of detecting Fe^{3+}.[32–35] Inspired by these studies, it is indicated that if the detection of biomolecules is

---

[a] *State Key Laboratory of Chemical Resource Engineering, Beijing Key Laboratory of Bioprocess, College of Life Science and Technology, Beijing University of Chemical Technology, Beijing 100029, China. E-mail: yangj@mail.buct.edu.cn*

[b] *College of Chemistry, Beijing University of Chemical Technology, Beijing 100029, China*

† Electronic supplementary information (ESI) available. See DOI: 10.1039/d1sd00015b

associated with Fe^{3+}, the combination of Fe^{3+} and AuNP@PTA will provide a chance to construct a new visual readout sensor.

Mesoporous silica nanoparticles (MSNs) are a class of widely known inorganic nanomaterials.[36] Due to their unique features including a high internal volume and narrow channels, MSNs are a versatile and promising platform for the loading of biomacromolecules or small molecules.[37,38] MSNs are definitely good containers for Fe^{3+} as well. Based on the above considerations, in this contribution, MSNs and AuNP@PTA were combined to explore a kind of colorimetric system, named as probe-labelled PEGylated AuNP@PTA@Fe^{3+}-loaded MSNs (Scheme 1). AuNPs, as an imaging agent, were prepared and stabilized using PTA, followed by the decoration of the probe-labelled poly(ethylene glycol) (PEG) *via* a thiol terminal group to bind with the AuNP surface for specially recognizing biomolecules (Scheme 1A). MSNs were regarded as a reservoir to load iron(III) ions and capped with the probe-labelled PEGylated AuNP@PTA through the electrostatic interaction between the negative PTA shell and the positive amine groups on the surface of MSNs (Scheme 1B).

Carbonic anhydrases (CAs, EC 4.2.1.1) are a class of critical enzymes that balance the reversible hydration of carbon dioxide to bicarbonate for human health and blocking endogenous chemistry.[39–41] Many CAs have been associated with neoplastic growth. In particular hypoxia-inducible CA IX and CA XII as well as the widely expressed CA II have been reported in certain tumors.[42–44] Overexpressed CAs have been known as an important class of analytes for tumor diagnosis. Sulfonamides have emerged as classical CA inhibitors which interact with a wide range of different cellular targets.[45] Sulfonamides specially binding to CAs have been gradually discovered and widely

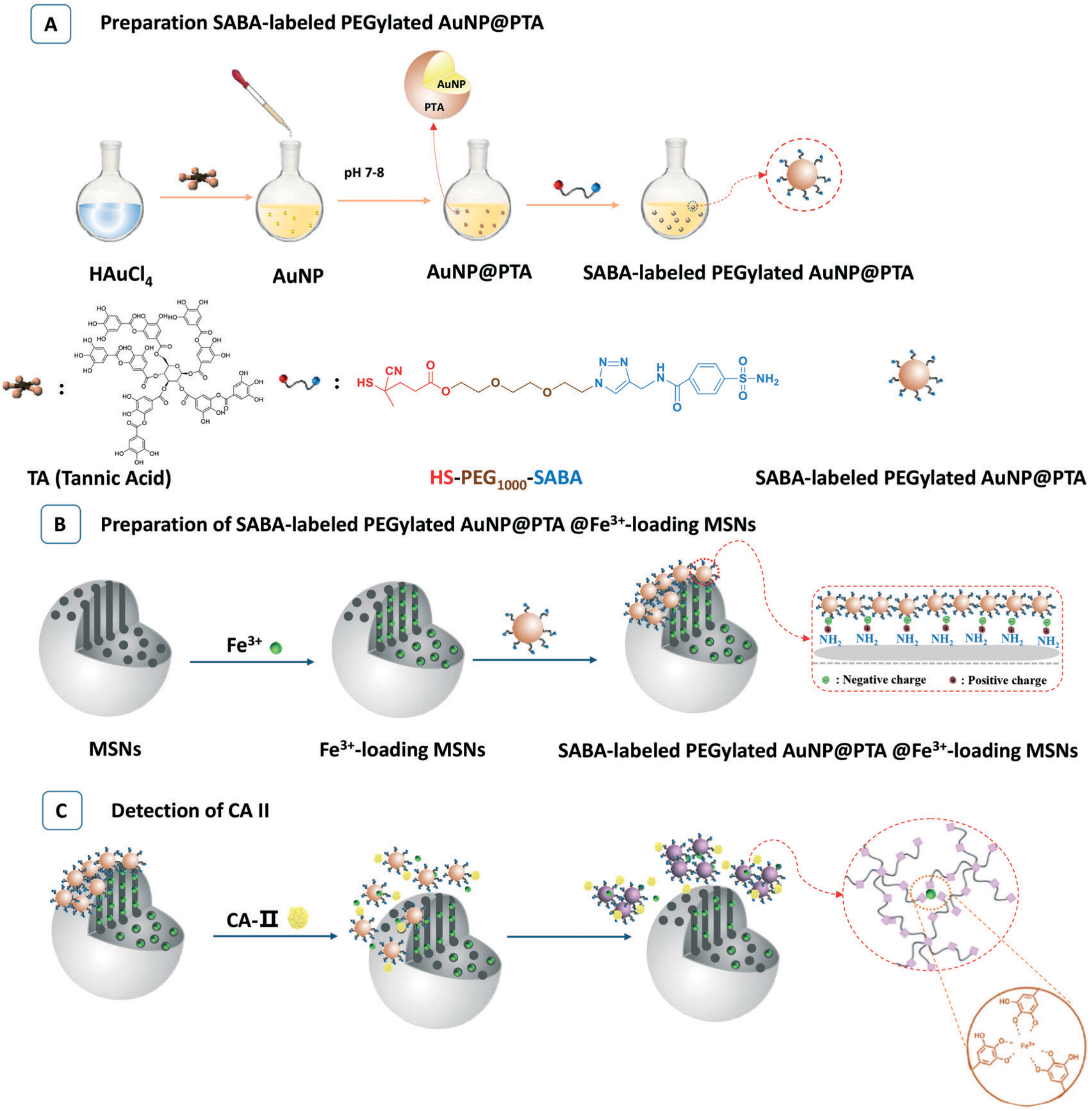

Scheme 1 The preparation procedures for SABA-labelled PEGylated AuNP@PTA@Fe^{3+}-loaded MSNs (A and B) and detection of CA II (C).

developed.[46,47] In this study, we selected isozyme CA II as the target analyte, and 4-sulfonamidebenzoic acid (SABA) was regarded as the probe molecule to link with the surface of AuNP@PTA through a PEG chain (Scheme 1A). Once the target CA II was presented, the stronger affinity of CA II and SABA compared to the electrostatic interaction between PTA and amine groups triggered the removal of gatekeeper AuNP@PTA from the surface of the MSNs (Scheme 1C). The iron(III) ions rapidly released from the MSNs were coordinated with PTA, leading to the aggregation of AuNPs and the color change. This visual readout sensor doesn't need any separation, and the operation is simple and convenient. With the aid of a UV-vis technique, such a detection system can provide some quantitative results as well.

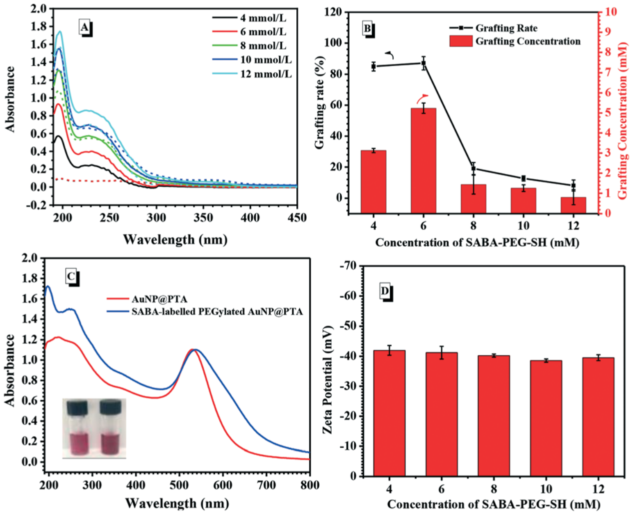

Fig. 1 (A) UV-vis curves of SABA-PEG-SH at different concentrations in the supernatant before (solid line) and after (dotted line) adding AuNP@PTA, [AuNP@PTA] = 0.356 μM, 10 mL. (B) The grafting efficiency and grafting concentrations of SABA-PEG-SH on AuNP@PTA. (C) Comparative UV-vis curves of AuNP@PTA before and after adding SABA-PEG-SH; the inset is the picture of the NP solutions before adding (left) and after adding SABA-PEG-SH (right). (D) Dependence of the zeta potential of SABA-labelled PEGylated AuNP@PTA on the given concentrations of SABA-PEG-SH.

Results and discussion

1. Characterization of the as-prepared SABA-labelled PEGylated AuNP@PTA probe

As reported,[48] a AuNP nanocomposite was synthesized by one-pot synthesis mixing of Au^{3+} and TA. Under the optimal conditions including [$HAuCl_4$] = 0.5 mM and [TA]/[$HAuCl_4$] = 2/1, the average diameter of the afforded AuNPs was 20 nm with unimodal dispersity (Fig. S1†). The nanoparticle solution exhibited a wine red color similar to that typical for Au colloids, and the UV-vis spectra of the AuNP solution show an extinction peak at around 550 nm (Fig. S2†). The solution pH was further investigated for the oxidation cross-linking of TA on the surface of the AuNP. As a result, with the pH increasing from 3.3 to 7.0, the zeta potential on the surface of the Au cores dramatically decreased from +17.5 ± 5.0 mV to −35.3 ± 4.0 mV, due to the oxidation of acidic galloyl groups by oxygen dissolved in the solution (Fig. S3†). The lowest zeta potential was observed at pH = 7.5–8.0, indicating the highest integration of the PTA shell onto the AuNP surface. Subsequently, the zeta potential rapidly increased at pH above 8.5, associated with PTA disassembling into smaller soluble molecules from the AuNP surface. These results were in good agreement with the previous reports.[49,50] Therefore, the optimal pH for AuNP@PTA synthesis was selected to be pH 7.8. As determined by TEM measurements (Fig. S4†), the size of spherical AuNP@PTA was averaged between 15 and 25 nm. Moreover, the centrifugation speed of 12 000 rpm was optimal for purifying and concentrating AuNP@PTA (Fig. S5†).

Based on it, the stable AuNP@PTA colloid solution was further labelled by SABA-PEG-SH. The hydroxyl groups at the both ends of PEG chain were respectively conjugated with SABA for recognizing the target CA II, and converted to thiol groups for anchoring on the surface of the AuNPs (Fig. S6–S14†). When the concentration of AuNP@PTA was maintained at 0.356 μM, SABA-PEG-SH at the determined concentration was incubated in the AuNP@PTA aqueous solution for 8 h and then centrifuged at 12 000 rpm for separation. The supernatant and initial SABA-PEG-SH solution were analysed by UV-vis spectroscopy, respectively. As a result, the characteristic absorbance of SABA-PEG-SH at 195 nm obviously changed after adding AuNP@PTA (Fig. 1A). When the concentration of SABA-PEG-SH was controlled at 6 mM or below, the UV-vis absorbance of the supernatant at 195 nm dramatically dropped in the presence of AuNP@PTA, indicating that all the SABA-PEG-SH conjugated onto the surface of AuNP@PTA. However, with an increase in the given concentration of SABA-PEG-SH to 8 mM or higher, a great amount of free SABA-PEG-SH remained in the supernatant, which was supported by the strong absorbance peak at 195 nm. The grafting efficiency of SABA-PEG-SH on the surface of AuNP@PTA was estimated by comparing the absorbance change at 195 nm after the addition of AuNP@PTA to the initial absorbance ($\Delta A/A_0$). As shown in Fig. 1B, the grafting rate was maximized to 87% when the concentration of SABA-PEG-SH was 6.0 mM, accordingly accompanied by about 5.2 mM SABA-PEG-SH on the resulting AuNP. Compared with AuNP@PTA dispersed in water, SABA-labelled PEGylated AuNP@PTA caused a very slight red-shift and broadening of the plasmon resonance peak (Fig. 1C).[51] SABA-labelled PEGylated AuNP@PTA still exhibited the characteristic wine red color. The zeta potential of the resulting nanoparticles remained at *ca.* −40 mV (Fig. 1D), close to that of AuNP@PTA, indicating the little impact of the SABA-PEG-SH grafting on the PTA shell on the surface of the AuNP core.

2. Characterization of the as-prepared Fe^{3+}-loaded NH_2-modified MSNs

MSNs were prepared according to a reported procedure,[52] and the TEM image shows the MSNs with a diameter of *ca.* 70 nm, in agreement with the DLS results (Fig. S15A†). The empty channels inside the MSNs were observed as well (Fig. S15B†). The Brunauer–Emmett–Teller (BET) nitrogen adsorption–desorption isotherms and Barrett–Joyner–Halenda (BJH) pore size distribution analysis were employed to confirm the mesoporous nature (Fig. 2A). A typical type-IV isotherm of the mesoporous structure was depicted in Fig. 2A, indicating an average pore diameter of 8.65 nm, a BET surface area of 1377.73 $m^2\ g^{-1}$ and a pore volume of 2.90 $cm^3\ g^{-1}$. The prepared MSNs with large pore volumes were suitable for Fe^{3+} loading. The surfaces of the bare MSNs were further amine-functionalized for electrostatic interaction with AuNP@PTA. Under the rigorous anhydrous conditions, amine modification was carried out in the presence of (3-aminopropyl)triethoxysilane (APTES), and the amination results were obtained by measuring the zeta potential. The negative charge of the bare MSNs according to their silanol group changed from −18.5 mV ± 1.51 to 10.6 ± 0.75 mV when the determined APTES was set at 85.5 μM (Fig. S16†). The shift toward a positive charge state suggested the successful amine modification of MSNs. With increasing the given concentration of APTES to 128 μM, the zeta potential of the modified MSNs slightly increased to 12.5 ± 1.56 mV, which is preferred for the electrostatic interaction with the PTA shell.

Fe^{3+}, as a trigger to induce the aggregation of AuNP@PTA for visual detection, was loaded into the mesoporous structure of the NH_2-modified MSNs by a passive diffusion method. The Fe^{3+}-loaded MSNs were washed and then dispersed in deionized water in order to remove free Fe^{3+} or Fe^{3+} near the surface of the MSNs. Because Fe^{3+} itself doesn't have any characteristic UV-vis absorbance, 5-sulfosalicylic acid dihydrate as a chromogenic agent was selected to complex with Fe^{3+} for optimizing the loading conditions. The absorbance difference of the characteristic peak at 420 nm in the presence and absence of NH_2-modified MSNs was determined to measure the loading efficiency by varying the initial Fe^{3+} concentrations. As a result, the loading concentration of Fe^{3+} in the MSNs increased first and then dropped with the initial Fe^{3+} concentrations increasing (Fig. 2B). When the initial Fe^{3+} concentration was 0.6 M, the loading concentration of Fe^{3+} in the MSNs reached the maximum as well as the loading efficiency, which was essential for sensitive target detection.

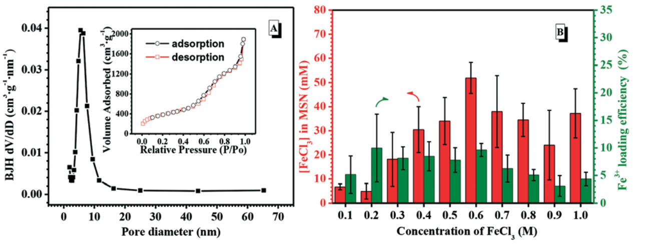

Fig. 2 (A) Pore diameter dispersity of the MSNs (inset: absorbance and desorption curves of the MSNs). (B) The Fe^{3+} loading concentrations and loading efficiency in the NH_2-modified MSNs ([NH_2-modified MSNs] = 4 mg mL^{-1}, 5 mL).

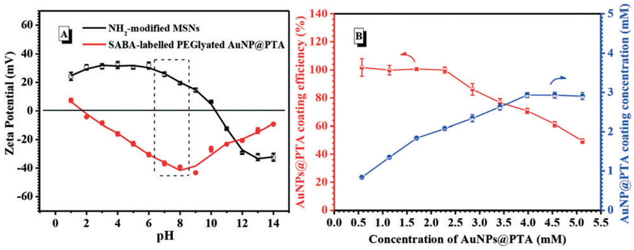

Fig. 3 (A) Zeta potential of the NH_2-modified MSNs and SABA-labelled PEGylated AuNP@PTA under different pH conditions ([NH_2-modified MSNs] = 4.0 mg mL^{-1}; [SABA-labelled PEGylated AuNP@PTA] = 0.359 mM). (B) Dependence of the AuNP@PTA coating efficiency and concentration for the NH_2-modified MSNs on the given SABA-labelled PEGylated AuNP@PTA concentrations ([NH_2-modified MSNs] = 0.3 mg mL^{-1}, 10 mL).

3. Characterization of SABA-labelled PEGylated AuNP@PTA-capped Fe^{3+}-loaded MSNs

The deprotonation of the PTA shell on the surface of the AuNP and protonation of amine-modified MSNs caused the increase in the efficiency of AuNP@PTA coating on the surface of the MSNs as a consequence of electrostatic interaction. The zeta potential of the NH_2-modified MSNs remained positive and constant below pH 6.0, but obviously decreased with the environmental pH further increasing, even becoming negative at pH above 10 (Fig. 3A). In contrast, the zeta potential of SABA-labelled PEGylated AuNP@PTA dropped to the minimum in the pH range of 1.0 to 8.0, and rapidly increased at pH above 8.5. The greater the charge

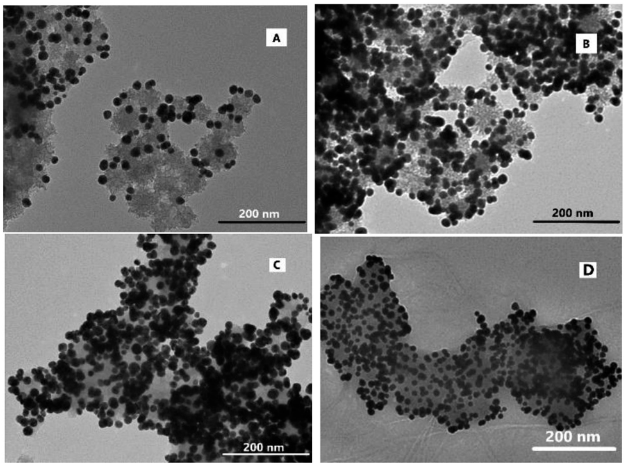

Fig. 4 TEM images of SABA-labelled PEGylated AuNP@PTA@Fe^{3+}-loaded MSNs at different given concentrations of SABA-labelled PEGylated AuNP@PTA: (A) 0.57 mM, (B) 2.85 mM, (C) 4.55 mM, and (D) 5.12 mM ([NH_2-modified MSNs] = 0.3 mg mL^{-1}).

disparity between AuNP@PTA and MSNs, the more favorable the AuNPs for electrostatically hybridizing onto the surface of MSNs. Therefore, the environmental pH at 7.5 was optimal for SABA-labelled PEGylated AuNP@PTA coating on the MSNs.

Besides, the coating efficiency of AuNP@PTA on the surface of the MSNs was affected by the given concentrations of AuNP@PTA as well. The UV-vis absorbance spectra of the SABA-labelled PEGylated AuNP@PTA solution at 550 nm before and after adding NH_2-modified MSNs were compared to measure the coating efficiency (Fig. S18†). As shown in Fig. 3B, nearly all the given AuNP@PTA was completely coated onto the surface of MSNs, thus keeping a coating efficiency of 100 percent when the concentration of the AuNPs was not more than 2.5 mM. With further increasing the initial concentration of the AuNPs, the coating efficiency started to drop, but the AuNP coating concentration on the surface of MSNs increased till a plateau was reached. The results of SABA-labelled PEGylated AuNP@PTA coating on the Fe^{3+}-loaded MSNs were observed by TEM as well. It is easily seen that the surface of the Fe^{3+}-loaded MSNs was partially coated by SABA-labelled PEGylated AuNP@PTA when the given concentration of the AuNPs was set at 0.57 mM (Fig. 4A). With the SABA-labelled PEGylated AuNP@PTA concentration increasing to 2.85 mM, the coating density of AuNP@PTA on the surface of the MSNs dramatically increased, but a small amount of bare-surface MSNs still remained (Fig. 4B). When the SABA-labelled PEGylated AuNP@PTA concentration was above 4.0 mM, the surface of the MSNs was well coated with AuNP@PTA (Fig. 4C and D). Thus, the initial concentration of SABA-labelled PEGylated AuNP@PTA was optimized to be 4.0 mM.

4. Detection assay of CA II using the SABA-labelled PEGylated AuNP@PTA@Fe^{3+}-loaded MSNs

In this assay, the signal readout was included such as SABA recognizing CA II, AuNP disassociating from the surface of

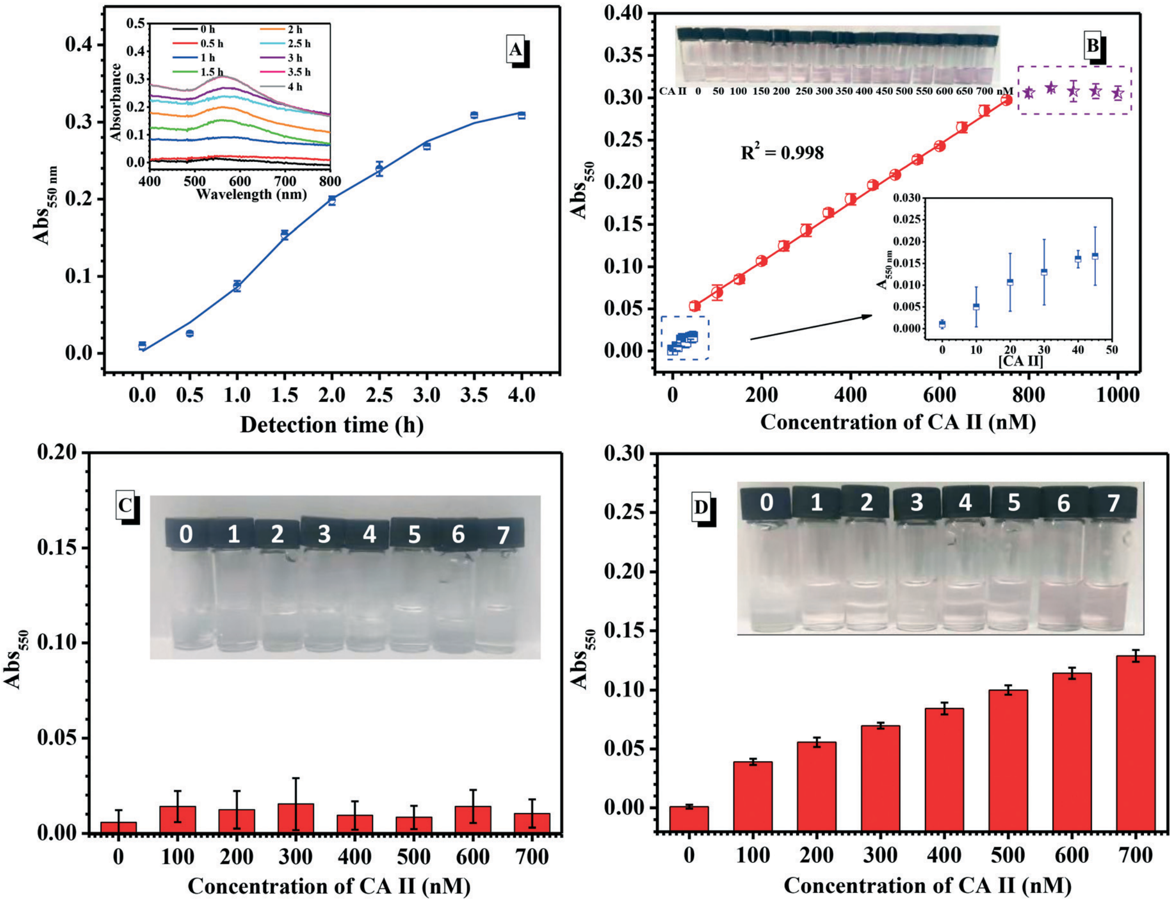

Fig. 5 (A) Dependence of the absorbance values of the SABA-labelled PEGylated AuNP@PTA@Fe^{3+}-loaded MSNs at 550 nm on detection time. Inset: The corresponding UV-vis spectra of CA II detected using the SABA-labelled PEGylated AuNP@PTA@Fe^{3+}-loaded MSNs. (B) The absorbance of the SABA-labelled PEGylated AuNP@PTA@Fe^{3+}-loaded MSNs at 550 nm at different CA II concentrations. The left upper inset shows the visual change at various concentrations of CA II. (C) The absorbance of the PEGylated AuNP@PTA@Fe^{3+}-loaded MSNs without SABA labelling at 550 nm at different CA II concentrations. Inset: The corresponding visual change at various concentrations of CA II from 0–700 nM. (D) The absorbance of SABA-labelled PEGylated AuNP@PTA@MSNs without Fe^{3+} loading at 550 nm at different CA II concentrations. Inset: The corresponding visual change at various concentrations of CA II from 0 to 700 nM ([Fe^{3+}-loaded MSN] = 0.3 mg mL^{-1}, SABA-labelled PEGylated AuNP@PTA = 4.0 mM, and the total volume of the detection system is 1 mL).

MSNs, Fe^{3+} escaping from the channels of MSNs and the aggregation of the AuNPs triggered by Fe^{3+} cross-linking with PTA. Therefore, the optimum detection time is essential to study the recognition of CA II. Under the above optimal conditions, UV-vis spectroscopy was used to monitor the absorbance change at 550 nm of the supernatant during CA II (700 nM) incubation with the SABA-labelled PEGylated AuNP@PTA@Fe^{3+}-loaded MSNs. Upon prolonging the time, the absorbance at 550 nm gradually increased, indicating that the aggregation of the AuNPs happened (Fig. 5A). The absorbance leveled off after 3.5 h incubation. Thus, 4 h-incubation would be carried out to evaluate the detection performance by exposing the SABA-labelled PEGylated AuNP@PTA@Fe^{3+}-loaded MSNs to different levels of CA II.

As shown in Fig. 5B, the absorbance peak of AuNP@PTA gently increased first as the concentration of the detected CA II approached 50 nM. Differently, the absorbance at 550 nm continuously and linearly increased, proportional to the CA II levels in the range of 50–700 nM. Notably, a significant color change from colorless to pale pink to pink-purple depending on various CA II concentrations was easily distinguished with the naked eye (inset in Fig. 5B). This was evidenced by the TEM result for the supernatant solution after detecting CA II, which showed that the AuNPs locally aggregated, but were not tightly, concurrently surrounded by a great amount of PTA (Fig. S20†). Upon further increasing the CA II concentration, the appearance of an absorbance plateau indicated the upper limit of detection, whereas the limit of detection (LOD) for the AuNP@PTA@Fe^{3+}-loaded MSNs was about 15 nM using a signal-to-noise ratio of 3.

In contrast, when CA II was added into the detection system using PEGylated AuNP@PTA@Fe^{3+}-loaded MSNs without SABA labelling, all the absorbance peaks of the supernatant at 550 nm were quite low in the CA II concentration range of 100–700 nM, and the colorless solution remained unchanged after 4 h detection (Fig. 5C). This strongly supported the recognition specificity of this colorimetric assay. In addition, when SABA-labelled PEGylated AuNP@PTA@MSNs without Fe^{3+} loading were used to detect CA II, it was found that the absorbance at 550 nm was much weaker than the detection system with Fe^{3+} loading at the same CA II concentrations, and there was no obvious color change even with 500 nM CA II. This indicated that Fe^{3+} could effectively enhance the sensitivity of this assay. Moreover, it is noteworthy that this mix-and-measure assay doesn't need any separation process. The incubation of the analyte and the detection system for a period of time was directly used to give the results.

To further confirm the specificity of the SABA-labelled PEGylated AuNP@PTA@Fe^{3+}-loaded MSN assay, we investigated the response of the sensor for 300 nM CA II, human serum albumin (HSA), β-2-microglobulin (β-MG), streptavidin (SA) and transthyretin (TTR), respectively (Fig. 6A). The experimental results clearly showed that the absorbance of CA II was much higher than those of the other proteins. The CA II showed an absorbance of approximately 0.12 at 550 nm, at which point we could distinguish the pink purple color with the naked eye. However, the other proteins exhibited low absorbance with no visual color change. Next, we evaluated whether the SABA-labelled PEGylated AuNP@PTA@Fe^{3+}-loaded MSN assay was capable of detecting CA II in a mixture of proteins. Using a mixture of HSA and CA II with varying feeding ratios from 0.25/1 to 1.25/1, it was clearly observed that the absorbance intensity in the presence of HSA was maintained, as well as that for CA II alone, even in excess of CA II (Fig. 6B). Identical results were obtained when β-MG was mixed with CA II, as shown in Fig. 6C. These results indicated the non-specific interaction of HSA, β-MG, SA and TTR, and the negligible influences of these external proteins on CA II detection. The SABA-labelled PEGylated AuNP@PTA@Fe^{3+}-loaded MSN assay showed good recognition specificity to CA II.

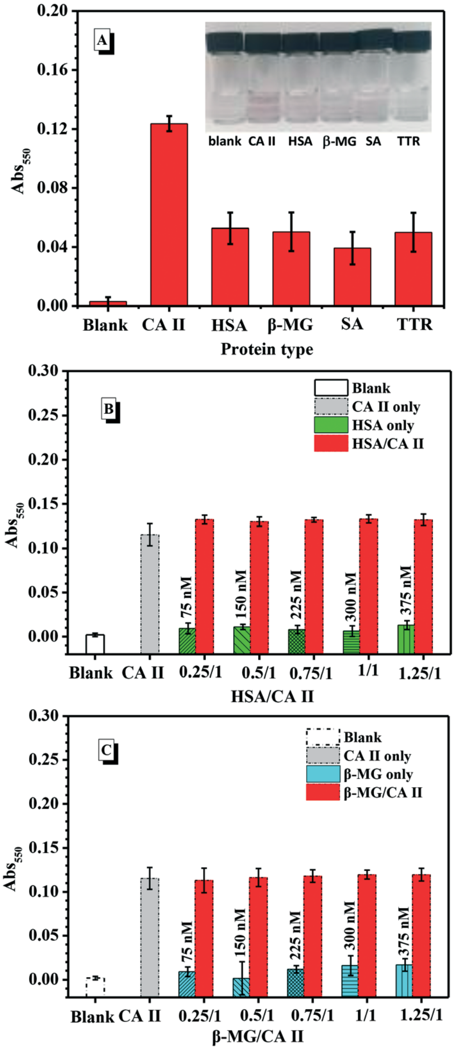

Fig. 6 (A) Detection results for various proteins using the SABA-labelled PEGylated AuNP@PTA@Fe^{3+}-loaded MSNs. Comparative results for the CA II and HSA mixture (B) and the CA II and β-GM (C) mixture in the presence of the SABA-labelled PEGylated AuNP@PTA@Fe^{3+}-loaded MSNs. [Fe^{3+}-loaded MSNs] = 0.3 mg mL^{-1}, [SABA-labelled PEGylated AuNP@PTA] = 4.0 mM, and [CA II] = 300 nM.

Conclusions

We have developed a sensitive protein sensor based on MSNs and AuNP nanocomposites. TA reduced the gold salt to form AuNP, oxidized itself into PTA, and assembled onto the AuNPs to form AuNP@PTA nanocomposites under slightly alkaline conditions. Under the optimal conditions including the environmental pH at 7.5, the initial Fe^{3+} concentration at 0.6 M and the given SABA-labelled PEGylated AuNP@PTA concentration of 4.0 mM, amine-modified MSNs loaded with the maximum amount of Fe^{3+} were entirely coated with SABA-labelled PEGylated AuNP@PTA. Relying on Fe^{3+} coordinating to the galloyl groups on PTA, a kind of colorimetric assay using SABA-labelled PEGylated AuNP@PTA@Fe^{3+}-loaded MSNs was explored for detecting CA II. The LOD for a visual color change from colorless to pale pink to pink-purple in the presence of CA II alone was as low as 50 nM, and the LOD with the aid of a UV-vis technique was about 15 nM using a signal-to-noise ratio of 3. Even in the presence of other proteins mixed with CA II, this assay still exhibited good specificity and sensitivity. Besides, this assay doesn't need any separation process, and the operation is simple and convenient. The combination of recognition molecules and analytes can be arbitrarily changed; thus, this assay will provide more opportunity to satisfy the versatile needs of protein detection.

Author contributions

Jing Yang: conceptualization, funding acquisition, project administration, and writing – review & editing. Jiale Pan: investigation and data curation. Junjiao Yang: TEM analysis. Shiman Yao: data curation.

Conflicts of interest

There are no conflicts to declare.

Acknowledgements

This work was supported by the National Natural Science Foundation of China (NSFC, Grant No. U1663227) and the Fundamental Research Funds for the Central Universities (PYBZ1810).

Notes and references

1 J. Rick, M. C. Tsai and B. Hwang, *Nanomaterials*, 2016, **6**, 5.

2 V. S. A. Jayanthi, A. B. Das and U. Saxena, *Biosens. Bioelectron.*, 2017, **91**, 15–23.

3 P. Miao, T. Zhang, J. H. Xu and Y. G. Tang, *Anal. Chem.*, 2018, **90**, 11154–11160.

4 X. Liu, R. L. Huang, R. X. Su, W. Qi, L. B. Wang and Z. M. He, *ACS Appl. Mater. Interfaces*, 2014, **6**, 13034–13042.

5 W. Y. Nie, Q. Wang, L. Y. Zou, Y. Zheng, X. F. Liu, X. H. Yang and K. M. Wang, *Anal. Chem.*, 2018, **90**, 12584–12591.

6 L. Y. Xia, M. J. Li, H. J. Wang, R. Yuan and Y. Q. Chai, *Anal. Chem.*, 2020, **29**, 14550–14557.

7 Z. H. Xu, H. Wang, J. Wang, W. Zhao, J. J. Xu and H. Y. Chen, *Anal. Chem.*, 2019, **91**, 12000–12005.

8 S. Azzouzi, Z. Fredj, A. P. F. Turner, M. B. Ali and W. C. Mak, *ACS Sens.*, 2019, **4**, 326–334.

9 B. Liu, J. Zhuang and G. Wei, *Environ. Sci.: Nano*, 2020, **7**, 2195–2213.

10 D. Zhu, B. Liu and G. Wei, *Biosensors*, 2021, **11**, 259.

11 H. Singh, A. Bamrah, S. K. Bhardwaj, A. Deep, M. Khatri, R. J. C. Brown, N. Bhardwaj and K. Kim, *Environ. Sci.: Nano*, 2021, **8**, 863–889.

12 Z. Yan, H. Yuan, Q. Zhao, L. Xing, X. Zheng, W. Wang, Y. Zhao, Y. Yu, L. Hu and W. Yao, *Analyst*, 2020, **145**, 3173–3187.

13 M. C. Daniel and D. Astruc, *Chem. Rev.*, 2004, **104**, 293–346.

14 K. Saha, S. S. Agasti, C. Kim, X. Li and V. M. Rotello, *Chem. Rev.*, 2012, **112**, 2739–2779.

15 F. Q. Li, H. Shao, J. J. Huang and A. J. Feng, *Sens. Actuators, B*, 2016, **226**, 506–511.

16 C. Song, X. Li, L. Hu, T. Shi, D. Wu, H. Ma, Y. Zhang, D. Fan, Q. Wei and H. Ju, *ACS Appl. Mater. Interfaces*, 2020, **12**, 8006–8015.

17 V. Uskokovic, *Nanomedicine*, 2020, **15**, 1719–1734.

18 A. Bigdeli, F. Ghasemi, N. Fahimi-Kashani, S. Abbasi-Moayed, A. Orouji, I. Jafar-Nezhad Zahra, F. Shahdost-Fard and M. R. Hormozi-Nezhad, *Analyst*, 2020, **145**, 6416–6434.

19 A. Mohamad, H. Teo, N. A. Keasberry and M. U. Ahmed, *Crit. Rev. Biotechnol.*, 2019, **39**, 50–66.

20 Y. Xianyu, J. Sun, Y. Li, Y. Tian, Z. Wang and X. Jiang, *Nanoscale*, 2013, **5**, 6303–6306.

21 Q. Zahra, Z. Luo, R. Ali, M. I. Khan, F. Li and B. Qiu, *Nanomaterials*, 2021, **11**, 840.

22 A. Rai and L. Ferreira, *Crit. Rev. Biotechnol.*, 2021, **41**, 186–215.

23 T. Dong, X. Ma, N. Sheng, X. Qi, Y. Chu, Q. Song, B. Zou and G. Zhou, *Sens. Actuators, B*, 2021, **327**, 128919.

24 C. Chang, C. Chen, T. Wu, C. Yang, C. Lin and C. Chen, *Nanomaterials*, 2021, **9**, 861.

25 G. Liu, M. Lu, X. Huang, T. Li and D. Xu, *Sensors*, 2018, **18**, 4166.

26 H. Aldewachi, T. Chalati, M. N. Woodroofe, N. Bricklebank, B. Sharrack and P. Gardiner, *Nanoscale*, 2018, **10**, 18–33.

27 Y. Zou, Z. Wang, H. Zhang and Y. Liu, *Biosens. Bioelectron.*, 2018, **122**, 205–210.

28 Y. Fang, J. Tan, H. Choi, S. Lim and D. Kim, *Sens. Actuators, B*, 2018, **259**, 155–161.

29 Y. Z. Cao, R. F. Zheng, X. H. Ji, H. Liu, R. G. Xie and W. S. Yang, *Langmuir*, 2014, **30**, 3876–3882.

30 T. Y. Kim, S. H. Cha, S. Cho and Y. Park, *Arch. Pharmacal Res.*, 2016, **39**, 465–473.

31 M. Sengani, A. M. Grumezescu and V. D. Rajeswari, *OpenNano*, 2017, **2**, 37–46.

32 H. Ejima, J. J. Richardson, K. Liang, J. P. Best, M. P. van Koeverden, G. K. Such, J. Cui and F. Caruso, *Science*, 2013, **341**, 154–157.

33 J. Wei, G. Wang, F. Chen, M. Bai, Y. Liang, H. Wang, D. Zhao and Y. Zhao, *Angew. Chem., Int. Ed.*, 2018, **57**, 9838–9843.

34 B. Li, J. J. Whalen, M. S. Humayun and M. E. Thompson, *Adv. Funct. Mater.*, 2020, **30**, 1907478.

35 B. J. Ortiz, J. Jennings, W. S. Gross, T. M. A. Santos, T. Lin, D. B. Weibel and D. M. Lynn, *Chem. Mater.*, 2021, **33**, 5401–5412.

36 E. Ilhan-Ayisig and O. Yesil-Celiktas, *Eng. Life Sci.*, 2018, **18**, 882–892.

37 N. Hao, L. Li and F. Tang, *Biomater. Sci.*, 2016, **4**, 575–591.

38 N. Ž. Knežević and J. Durand, *Nanoscale*, 2015, **7**, 2199–2209.

39 A. Nocentini, D. Vullo, G. Bartolucci and C. T. Supuran, *Bioorg. Med. Chem.*, 2016, **24**, 3612–3617.

40 G. Chen, A. Heim, D. Riether, D. Yee, Y. Milgrom, M. A. Gawinowicz and D. Sames, *J. Am. Chem. Soc.*, 2003, **125**, 8130–8133.

41 S. Nag, K. Manna and K. D. Saha, *RSC Adv.*, 2019, **9**, 8025–8038.

42 S. Pastorekova, S. Parkkila and J. Zavada, *Adv. Clin. Chem.*, 2006, **42**, 167–216.

43 S. Pastorekova, M. Zatovicova and J. Pastorek, *Curr. Pharm. Des.*, 2008, **14**, 685–698.

44 S. Parkkila, J. Lasota, J. A. Fletcher, W. B. Ou, A. J. Kivela, K. Nuorva, A. K. Parkkila, J. Ollikainen, W. S. Sly and A. Waheed, *et al.*, *Mod. Pathol.*, 2010, **23**, 743–750.

45 J. Drew, *Science*, 2000, **287**, 1960–1964.

46 R. Bashir, S. Ovais, S. Yaseen, H. Hamid, M. S. Alam, M. Samim, S. Singh and K. Javed, *Bioorg. Med. Chem.*, 2011, **21**, 4301–4305.

47 A. Maresca, C. Temperini, L. Pochet, B. Masereel, A. Scozzafava and C. T. Supuran, *J. Med. Chem.*, 2010, **53**, 335–344.

48 T. Zeng, X. L. Zhang, Y. Y. Guo, H. Y. Niu and Y. Q. Cai, *J. Mater. Chem. A*, 2014, **2**, 14807–14811.

49 L. Guo, A. R. Ferhan, H. Chen, C. Li, G. Chen, S. Hong and D. Kim, *Small*, 2013, **9**, 234–240.

50 M. Grzelczak, J. Perez-Juste, P. Mulvaney and L. M. Liz-Marzan, *Chem. Soc. Rev.*, 2008, **37**, 1783–1791.

51 S. Christau, T. Moeller, J. Genzer, R. Koehler and R. Klitzing, *Macromolecules*, 2017, **50**, 7333–7343.

52 M. Aghayan, A. Mahmoudi, M. R. Sazegar and F. Adhami, *J. Mater. Chem. B*, 2021, **9**, 3716–3726.